Chapter 4

Parameter study

In the previous chapter the geometric models used in this study were introduced, starting with the magnetic field geometry which underlies them. These models are based on the physical models discussed in Section 2.5 and describe only where the emission comes from in the magnetosphere, and not how this emission is produced. The various tools necessary for extracting useful results from these models were also introduced (see Section 3.5). In this chapter these tools are employed to investigate the effects of different specifications of the input parameters on the predictions yielded by these models. The goal of this parameter study is to provide a useful qualitative understanding of the geometric models, which will aid in the interpretation of the results obtained in Chapter 6.

In the geometric γ-ray models used in this study the parameters specifying the gap width W and gap extent (extending from a minimum radius $R_{\rm min}$ up to a maximum radius $R_{\rm max}$) are fixed for all the pulsars considered, while the pulsar period used to generate the LC predictions is fixed for each individual pulsar. For the radio case both the period and period derivative are fixed for each individual pulsar. The radio and γ-ray models give predictions for the geometric parameters α (the inclination angle) and ζ (the observer angle) which describe the configuration of the pulsar system and the observer's orientation with respect to the rotation axis. Thus three sets of parameters can be distinguished: those fixed beforehand for each pulsar (P, $\dot{P}$), those fixed beforehand for each model (W,$R_{\rm max}$), and those yielded by the geometric models (α, ζ), after obtaining best-fit LCs. The process by which these predictions are obtained is discussed in Chapter 5.

4.1 Inclination and observer angles: constructing a γ-ray atlas

The basic pulsar system, in a geometric sense (as depicted in Figure 3.3), consists of a central star rotating about its rotation axis and an accompanying magnetic field inclined at an angle α with respect to the rotation axis. This angle differentiates individual pulsar systems. The angle at which the observer is situated with respect to the rotation axis is called the observer angle ζ. Different values for this angle correspond to separate LC predictions for a single pulsar system. Thus, a single LC prediction from the geometric models is characterised by the values of these two geometric parameters, and consequently the range of these parameters constitute the solution space within which this study aims to find fits to the LC observations of the relevant pulsars. A related quantity is the impact angle $\beta = \zeta - \alpha$, which is the smallest angle between the observer's line of sight and the magnetic axis.

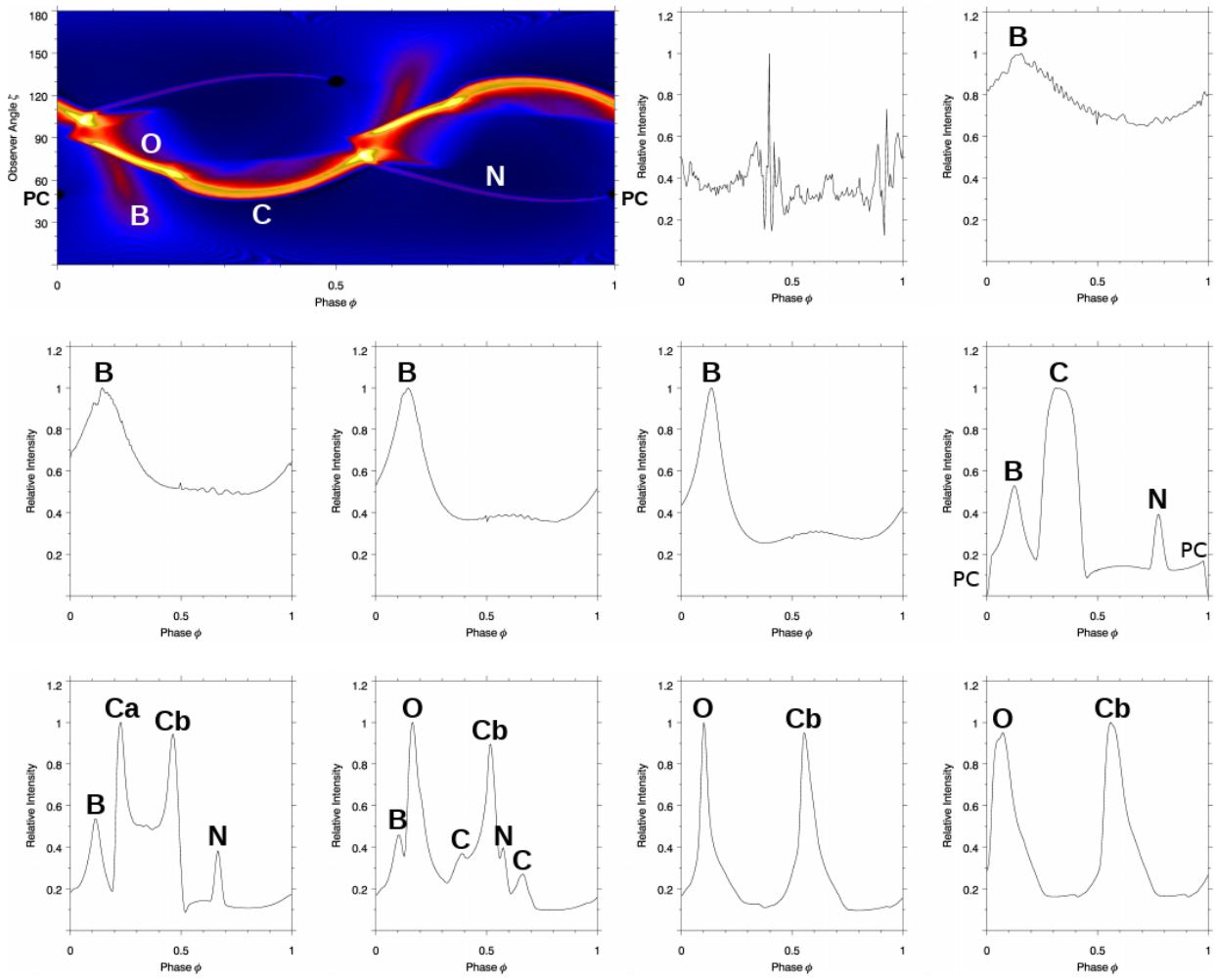


Figure 4.1: A TPC phaseplot for $\alpha = 50°$ accompanied by its corresponding LCs which are produced by taking constant-ζ cuts in 10° steps between $\zeta = 0°$ and 90°. The labels indicate the features on the phaseplot associated with each of the features on the LCs.

To study how α and ζ influence the LCs produced by the OG and TPC models, so-called atlases are constructed. For the purposes of this study, an atlas is simply a set of sample LCs for a grid in (α, ζ)-space at a chosen resolution, with α increasing left-to-right, and ζ increasing bottom-to-top (e.g., Figure 4.4). All angles are in degrees. In later chapters the atlases will be expanded to show both radio and γ-ray LCs.

4.1.1 A single column of an atlas: constant α, various ζ

Figure 4.1 shows a TPC phaseplot corresponding to $\alpha = 50°$, as well as the set of LCs corresponding to incrementally larger ζ values, starting at $\zeta = 0°$ and going up to $\zeta = 90°$ in steps of 10°. Considering these LCs in the context of the phaseplot, one can get a sense of which features on the phaseplot are responsible for the various peaks on the LCs. It must be kept in mind, however, that for each LC the emission intensity is normalised so that the strongest peak has a relative intensity of unity, which means that care must be taken not to make direct comparisons between LCs as to the relative peak intensities.

Comparing the LC at $\zeta = 0°$ to the phaseplot, all the major features on the phaseplot are

missing, and therefore the structure of this LC is related to the resolution chosen for the numerical model itself. The emission producing this LC can thus be considered to be noise. From $\zeta = 10°$ and onward structures begin to emerge. The first feature to be seen as ζ is increased is the "bump" B, which is the only phaseplot feature visible all the way up to $\zeta = 40°$. As ζ increases, the intensity of the peak associated with B increases relative to the rest of the LC, and it moves slightly earlier in phase due to the "negative slope" of B. At $\zeta = 50°$ four distinct features are discernible on the LC: three variably intense peaks, and a fall to zero in intensity at both ends of the LC. The earliest of these three peaks is again the peak associated with B. The middle peak is associated with the caustic C, with the cut producing this LC being tangential to this feature. The last of the three peaks appears as a result of the cut intersecting the notch line N on the phaseplot. As can be seen on the phaseplot, the intensity of the emission on C is much higher than that of B, which leads to the peak associated with C dominating the peak associated with B in the LC. The drop to zero intensity at both $\phi = 0$ and $\phi = 1$ is due to the PC (where it is assumed that no emission is generated at the PC on the stellar surface) as $\alpha = \zeta$ for this LC. The peak associated with C can be traced to $\zeta = 60°$, where C is no longer being cut tangentially, but farther up (higher ζ) on the phaseplot, producing two peaks (labelled Ca and Cb on the relevant LCs) with accompanying bridge emission between them. At larger ζ, this association between the two peaks (corresponding to the two different phases where the same caustic is cut) becomes less clear due to the bridge emission becoming very low. At $\zeta = 80°$ the two peaks can no longer be associated based solely on the LC, as there is almost no bridge emission. The last of the three peaks at $\zeta = 50°$ (associated with N), is present up to $\zeta = 70°$, where a transition from one feature (N) on the phaseplot to another, the so-called overlap O, occurs. Here, the small feature just after the second caustic peak is associated with N, while the last peak is produced by cutting the small tail of the $\zeta < 90°$ caustic. At $\zeta = 70°$, a small peak between the two caustic peaks appears which is associated with a very subtle feature just interior to C on the phaseplot.

Taking all these features and their movement on the LC into account as one increments ζ, one can interpret the differences in the shapes of LCs at different ζ's for a given α. The next step is to understand how the existence, shape, and position of these features are influenced when different values for α are considered.

4.1.2 Change across columns of a γ-ray atlas: columns as phaseplots

As illustrated in the previous section, multiple LCs can be extracted from a single phaseplot. The LCs shown in Figure 4.1 correspond to a single column of the TPC atlas. Thus each column of the atlas can be represented by a single phaseplot, with the differences between LCs in different columns being summarised by the differences between the phaseplots corresponding to those columns. Here the changes in the phaseplots as α increases from 0° to 90° are considered.

In the first pane in Figure 4.2, where $\alpha = 0°$, the only significant effect generating the phaseplot's structure is that of aberration, as discussed in Section 3.4. If the effect of this aberration were ignored the emission on the phaseplot would be more evenly distributed across ζ, but due to the higher corotation velocities nearer to the light cylinder the emission directions of the photons are aberrated. This aberration competes with the geometry of the magnetic field, with the outer edges of the broad caustic band on the phaseplot (between 70° and 110°) corresponding to the largest

ζ at which emission associated with the pole at $\zeta = 0°$ is seen. The thin zero emission bands at $\zeta = 0°$ and $\zeta = 180°$ are associated with the PCs.

As α is incremented, more structure emerges as the effect of time-of-flight delay becomes important. Four changes are present in the $\alpha = 10°$ phaseplot: the appearance of the bump trailing the PC; the stretched dark spot associated with the PC, centred around $\zeta = 10°$; the deformed shape of the intense central band, which is now more sinusoidal; and that the very intense band (in yellow) is no longer uniformly intense, but follows a similar pattern of intensity as the bump with respect to ϕ. The change in shape and position of the PC is easily understood geometrically, and proceeds uniformly for each step in α. The shape and effect of the actual PC is almost identical at a given α, but seems dramatically different in the progression of Figure 4.2 due to the effects of the mapping, discussed in Section 3.5.1. As discussed in Section 3.4, the effects of time-of-flight and aberration cause a bunching in phase of emission trailing the PC, as well as a spreading of emission in phase leading the PC.

The phaseplots at $\alpha = 20°$ and $\alpha = 30°$ (panes (c) and (d)) show that the features which appeared at $\alpha = 10°$ simply become more pronounced, with the intense bands almost completely cancelled out in the portions leading the PCs for $\alpha = 30°$. It is clear that the caustic effect is not limited to the very intense part of the broader band bounded by the two yellow bands, but operates on the inner portion as well. It is, however, only from $\alpha = 30°$ and onward that a part of what used to be the very intense bands at the edges of the broad band is less intense than the inner part of the broad band, e.g. at $0.2 < \phi < 0.5$ and $90° < \zeta < 110°$.

From $\alpha = 40°$ and onward the line associated with the notch starts appearing for the first time, extending from the leading edge of each PC. Another feature, O, related to N, also becomes apparent at this point. It initially only affects the apparent shape of the caustic, but becomes quite relevant at $50° < \alpha < 80°$, where it is responsible for a significant peak on the LCs with $60° < \zeta < 90°$. At $\alpha = 40°$ and $\alpha = 50°$ the previously separate features of the bump (B) and "horizontal" caustic (C) start to merge. This fusion becomes very clear when looking at the even higher α phaseplots. The effects discussed thus far turn out to be the only ones present throughout the rest of the phaseplots.

Turning now to the OG phaseplots (Figure 4.3), it can be seen that they are very similar. The main difference is that, in the OG case, no emission associated with a specific pole originates below the null-charge surface $R_{\rm NCS}$ (at $\Omega \cdot \boldsymbol{B} = 0$, i.e., $\zeta = 90°$). This results in many of the features present in the TPC case being absent in the OG case, such as the bump, the PC, and the notch line. This doesn't mean that the effects responsible for these features are also absent in the OG case. As can be seen at high α, e.g. $\alpha = 80°$, the high-altitude overlap associated with the bunched polar magnetic field lines, as well as the caustics brought about by the effects of time-of-flight and aberration, are still present. Another difference between the OG and TPC models visible on the phaseplots is that the caustics in the OG case tend to be slightly interior to their locations on the corresponding TPC phaseplots. This is due to the difference in gap position between the two geometries, and is discussed in more detail in Section 4.3.3. It is also very important to notice that at all α in the OG case there are large portions of the phaseplot from which no emission is observed. This serves very well to illustrate which emission originates from low altitudes (below $R_{\rm NCS}$) in the TPC case, and helps one acquire a better understanding of the origins of the different

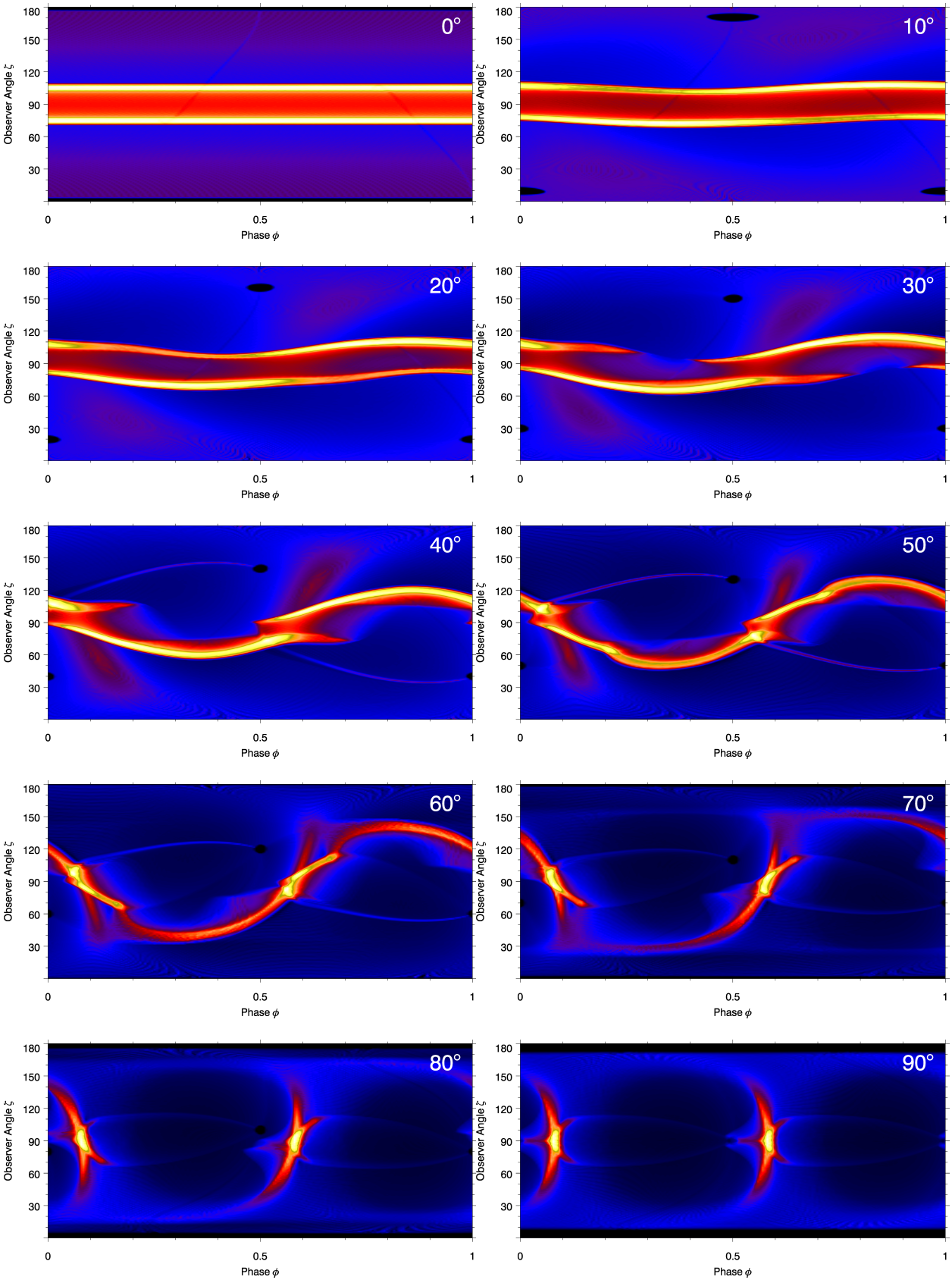


Figure 4.2: Phaseplots for α between 0° and 90°, stepping in increments of 10°, for the TPC case.

features on the phaseplots in both cases.

4.1.3 The γ-ray atlases as a whole

Upon considering the progression from phaseplot to phaseplot just discussed, one can now understand more thoroughly why the atlases in Figures 4.4 and 4.5 look the way they do. Moving from the bottom-left corner of the TPC atlas upward towards the top-right, for the first few steps ([10°,10°], [20°,20°], [30°,30°], [40°,40°]; and roughly their accompanying top-left to bottom-right diagonals) the most significant peak in the LCs is that due to the bump. This means that these LCs are basically characterised by a single broad peak early in phase lagging the fiducial plane by about 0.2 in phase, and by about 0.1 in phase at larger α and ζ. In this region the constant-ζ cuts are consistently lower on the phaseplots than the main caustic. This means that the only significant phaseplot feature is B. Stepping even farther away from the origin new phaseplot features become significant, e.g., the caustic and the notch line. The LCs at [40°,60°], [50°,50°], and [60°,40°] are very good examples of profiles where the caustic is cut tangentially and dominates the LC. In all three cases a peak associated with the bump can be seen, but it is only 30% to 50% as intense as the peak associated with the tangential caustic cut. It is important to note that the LCs in the atlas displaying tangential caustic cuts do not lie strictly on a top-left to bottom-right diagonal, but deviate from it. For the range in α from 40° to 70°, a top-left to bottom-right diagonal from [40°,60°] to [70°,30°] is, however, a good approximation.

Stepping past this approximate band of single-peaked profiles, more complex LCs are encountered. The majority of the LCs, though, have the characteristic that they are roughly two-peaked, and that those two peaks are associated with a cut of the caustic higher up on the phaseplot than a tangential cut. At $\alpha > 60°$ the leading peak arising from the caustic cut becomes indistinguishable from the peak associated with the bump, as the bump and the caustic essentially become one feature on the phaseplot (compare, e.g., [60°,50°] and [70°,50°]). Therefore, the two peaks on these profiles tend to be farther apart as one steps farther from the origin. The overlap shows up as a distinct feature just trailing the two caustic peaks on the LCs at $\zeta = 70°$ for $\alpha > 60°$, and is roughly confined to this ζ value. The last features that need to be noted, the effects of which can be traced through the atlas, are the PC and associated notch line. These affect the atlas only marginally. The PC's effect is visible as a sharp drop to zero at $\phi = 0$ and $\phi = 1$ in the profiles on the $\alpha = \zeta$ diagonal, while the notch line is responsible for a small peak in the profiles with positive β (< 20) between approximately [40°,40°] and [70°,70°].

The OG atlas, shown in Figure 4.5, is strikingly different. The most significant difference is that the pulsar is not visible over a large portion of the atlas. This is due to the fact that no emission occurs below the null-charge surface in this model (see Section 2.5). This portion of the atlas coincides almost exactly with that portion on the TPC atlas over which the bump was the only significant feature in the TPC case. The further progression of the atlas is somewhat similar to the TPC case, initially with narrow, single-peaked profiles, and then progressively wider two-peak profiles (for increasing α and ζ). These two-peaked profiles are generally characterised by having a leading peak which is considerably less intense than the trailing peak. This can be understood by noting that the caustic emission originating from below $R_{\rm NCS}$ in the TPC case is not present in the OG case. Considering the corresponding phaseplots, the leading peaks in the LCs in the upper

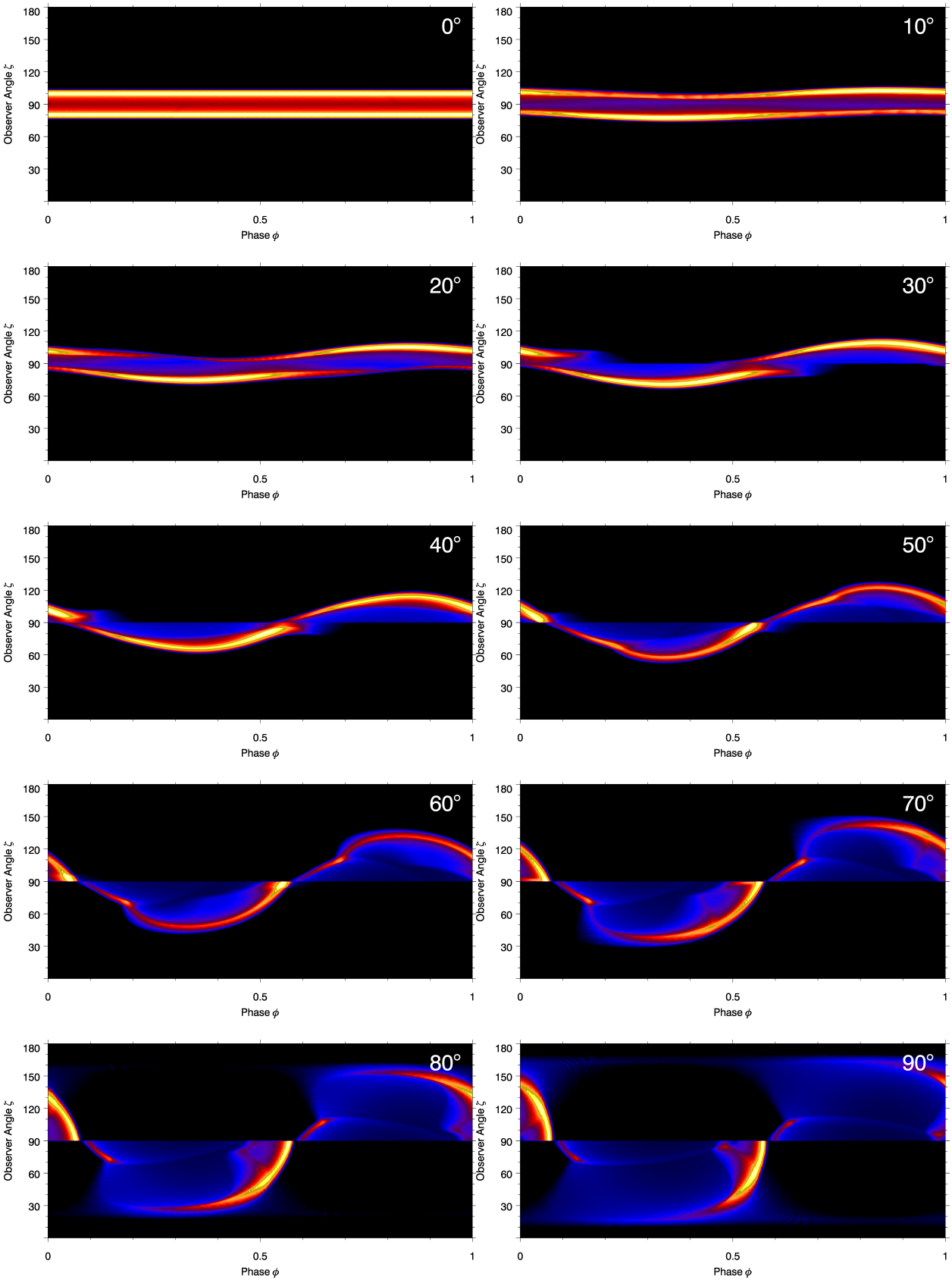


Figure 4.3: Phaseplots for α between 0° and 90°, stepping in increments of 10°, for the OG case.

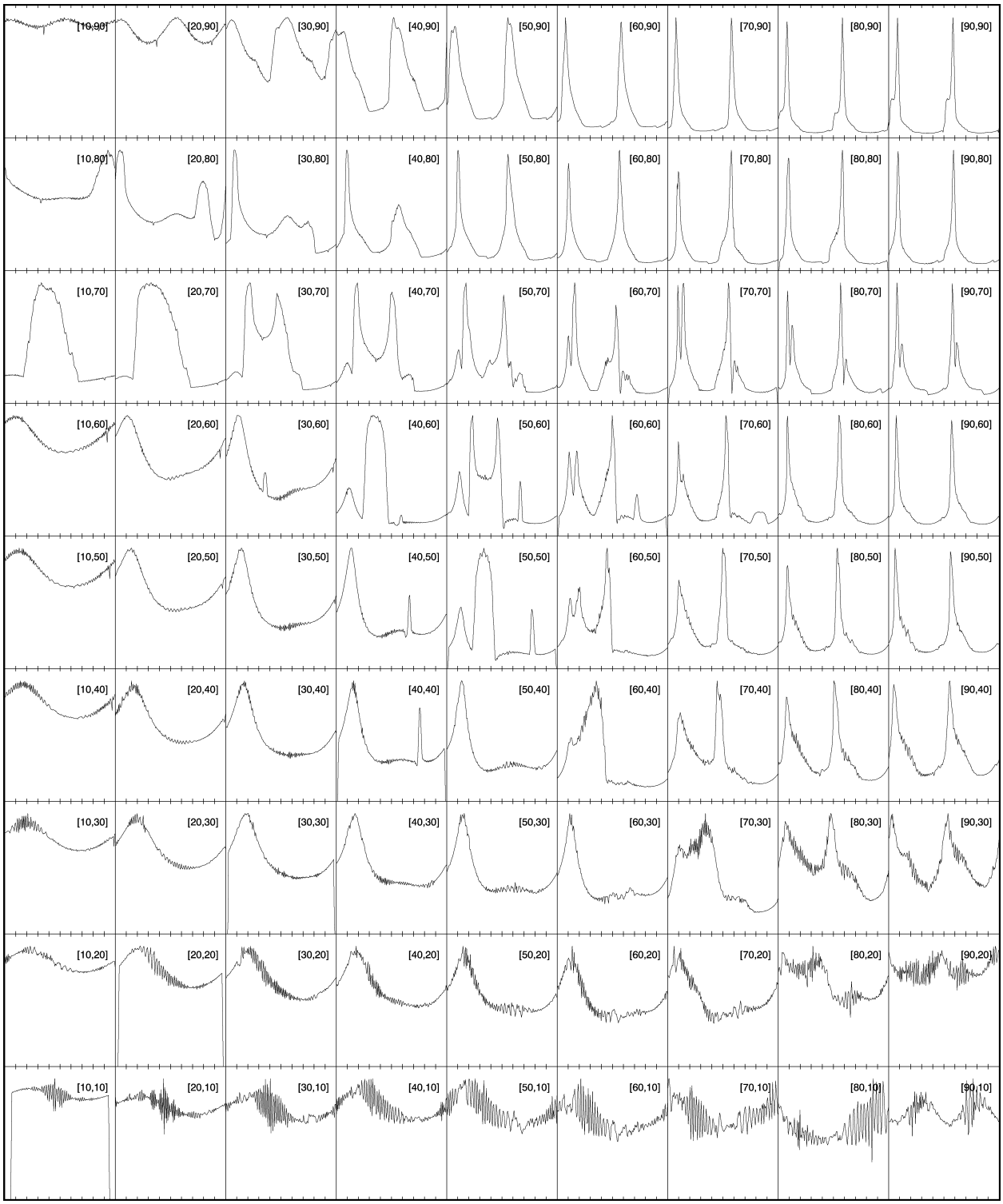


Figure 4.4: Atlas of LCs with a resolution of 10° in α and ζ for the TPC model. The value of α increases from left-to-right, while ζ increases from bottom-to-top.

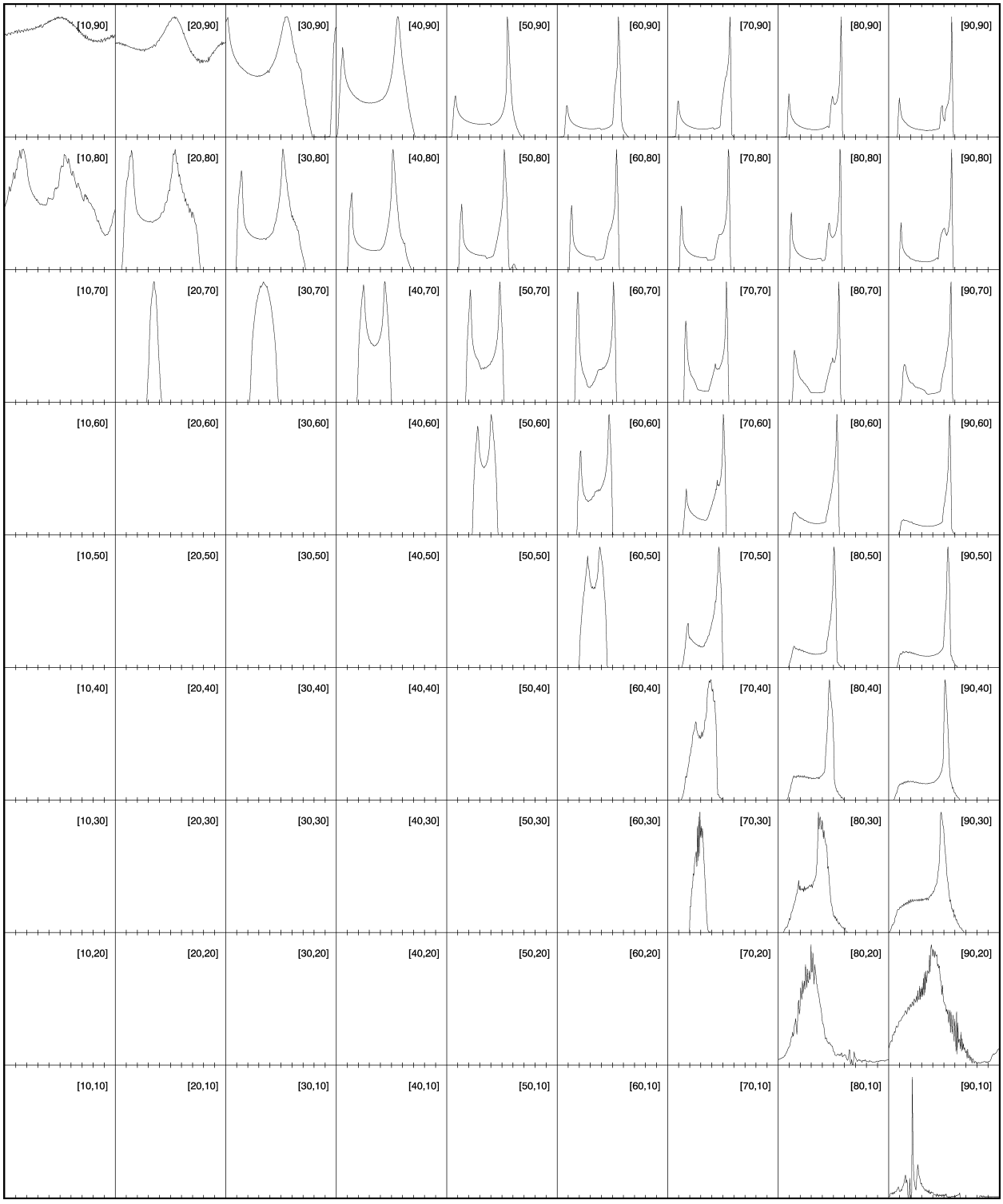


Figure 4.5: Atlas of LCs with a resolution of 10° in α and ζ for the OG model.

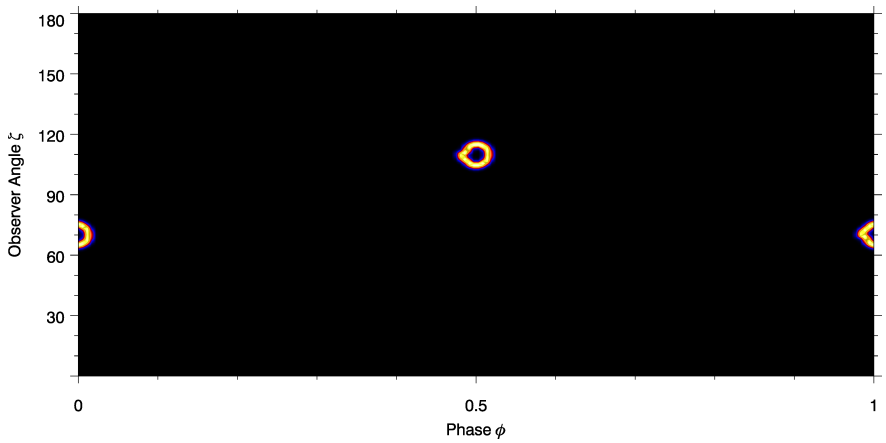


Figure 4.6: A sample radio phaseplot, with the characteristic ring of radiation roughly centred on the PC. For this phaseplot $\alpha = 70°$.

right of the OG atlas are wholly attributable to the overlap, with no caustic contribution.

Another striking feature of the OG atlas is that in the majority of the LCs no emission is observed over a potion of the pulsar's rotation, i.e., there is an absence of off-peak emission. This is in contrast with the trend seen on the TPC atlas where emission is observed over the whole rotation and over the whole atlas, barring those LCs on the $\alpha = \zeta$ diagonal where the PC is cut.

4.1.4 The radio atlas

In Figure 4.7 it can be seen that the radio atlas is, as expected, much simpler than that of the γ-ray emission, with the LCs all lying along the $\alpha = \zeta$ diagonal. The LCs farthest from the diagonal are single-peaked, while those on the diagonal are two-peaked. This can be easily understood by considering the typical shape of the radio phaseplot shown in Figure 4.6, and the fact that the ring is always centred on the PC. The single-peak profiles are produced when ζ is close enough to α to produce cuts tangential to the ring, while the two-peak profiles are produced when the ring is cut through the middle.

Besides these characteristics, it is of interest to consider what happens when the pulsar is nearly orthogonal, i.e., when α approaches 90°. On a typical radio phaseplot one full ring at $[0.5, 180° - \alpha]$ can be seen, and two half rings at $[0, \alpha]$ and $[1, \alpha]$. As α increases, the two half rings move upward on the phaseplot, while the full ring moves down. When $(180° - \alpha)$ becomes less than the ζ-extent of the rings, both the full ring and the two half rings can be seen on the same LCs (see, e.g., the LCs in the upper right on the atlas, where more peaks are visible).

The last important characteristic is that of the broader peaks at the lower left end of the diagonal. As discussed in Section 3.5.1, this is a purely geometric effect, and it can be understood by considering the sphere containing the annulus from which the emission originates, which is centred on the NS. On this sphere each observer angle corresponds to a different line of constant colatitude, with the lines associated with lower ζ being shorter than those corresponding to larger ζ. The angular size of the annulus of radiation, however, doesn't change considerably as α is varied, which means that for a similar impact angle $\beta = \zeta - \alpha$, the fraction of the rotation over which emission will be observed is larger for smaller ζ (this has also been referred to as the 'small-circle effect'). It is slightly countered by the increase in angular size of the annulus as α is increased, but

this effect is small.

4.2 Magnetospheric structure: static dipole vs. retarded dipole field

The geometric γ-ray models used in this study assume, as the basis for their basic topology, the retarded dipole model for the magnetic field (see Section 3.1). In this section the effect of the choice of magnetic field is illustrated by investigating what the phaseplots would look like if a simple static dipole field is employed.

Figure 4.8 shows a set of phaseplots as function of α for the static dipole, comparable to those shown in Figure 4.2 for the retarded dipole. At $\alpha = 0°$ the two magnetic fields produce almost identical phaseplots, both exhibiting black bands of no emission at $\zeta = 0°$ and $\zeta = 180°$ on the phaseplots, marking the PC positions.

Increasing α to 10°, very similar development in phaseplot structure to that of the retarded dipole commences, although it is subtly different. The first signs of a caustic presenting itself around 0.6-0.8 in phase can be seen in the upper half of the phaseplot at around $\zeta = 160°$, but it isn't as intense as in the previous case. Furthermore, the most intense parts of the yellow bands are closer to $\phi = 0.5$ than for the retarded dipole case, and the bands are not as thick. Increasing α again (say, to 30°), it can be seen that it is not only the emission contributing to the yellow bands which is bunching at earlier phases than in the retarded case, but also the emission responsible for the bump. This bump is also less intense relative to the maximum intensity in this phaseplot. Another difference is apparent, in terms of the shape of the yellow bands.

Increasing α again, through 40° and up to 50°, the bump B and caustic C begin to merge, and much of the emission in the broader band fades. This is a much simpler process than was seen in the retarded case, where the effect of the notch in the PC field lines was important. Significantly, the caustics in the static dipole case do not extend to as low ζ as they do in the retarded dipole case. This means that stronger LCs will be seen over a larger range of ζ values for the retarded dipole case than for the static dipole case. No features like the line N associated with the PC, or like the overlap O, can be seen.

Considering the phaseplots for α from 60° to 90°, a simple progression to a tear-shaped phaseplot at $\alpha = 90°$, with no new features, becomes apparent. Tangential cuts to the caustics only occur around 0.35 in phase in the static case, as opposed to 0.30 in the retarded case (for $30° < \alpha < 80°$), and are also generally found at higher ζ in the static case. It is also important to note that portions of the phaseplots in these last frames are not filled with emission, which means that there exists a set of ζ for each of the corresponding α values for which γ-rays will not be observed, e.g., $\zeta = 0°$ to 50° for $\alpha = 90°$.

4.3 The γ-ray parameters

4.3.1 Pulsar period

Figures 4.9 and 4.11 illustrate the effect of the pulsar's period P on the resulting phaseplots and LCs for the TPC case. The only notable effect is that the feature associated with the PC (the dark

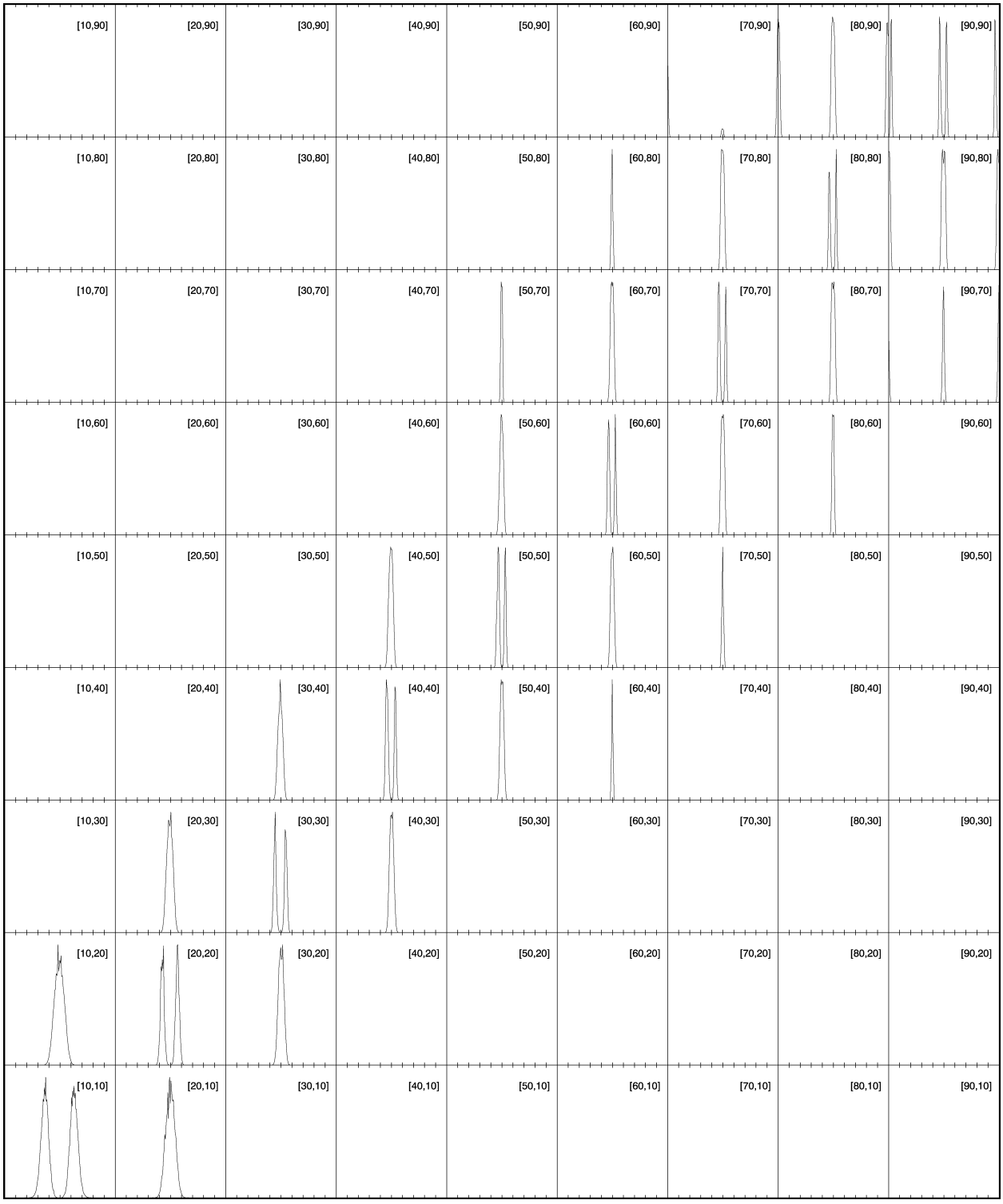


Figure 4.7: Atlas of LCs with a resolution of 10° in α and ζ for the radio model.

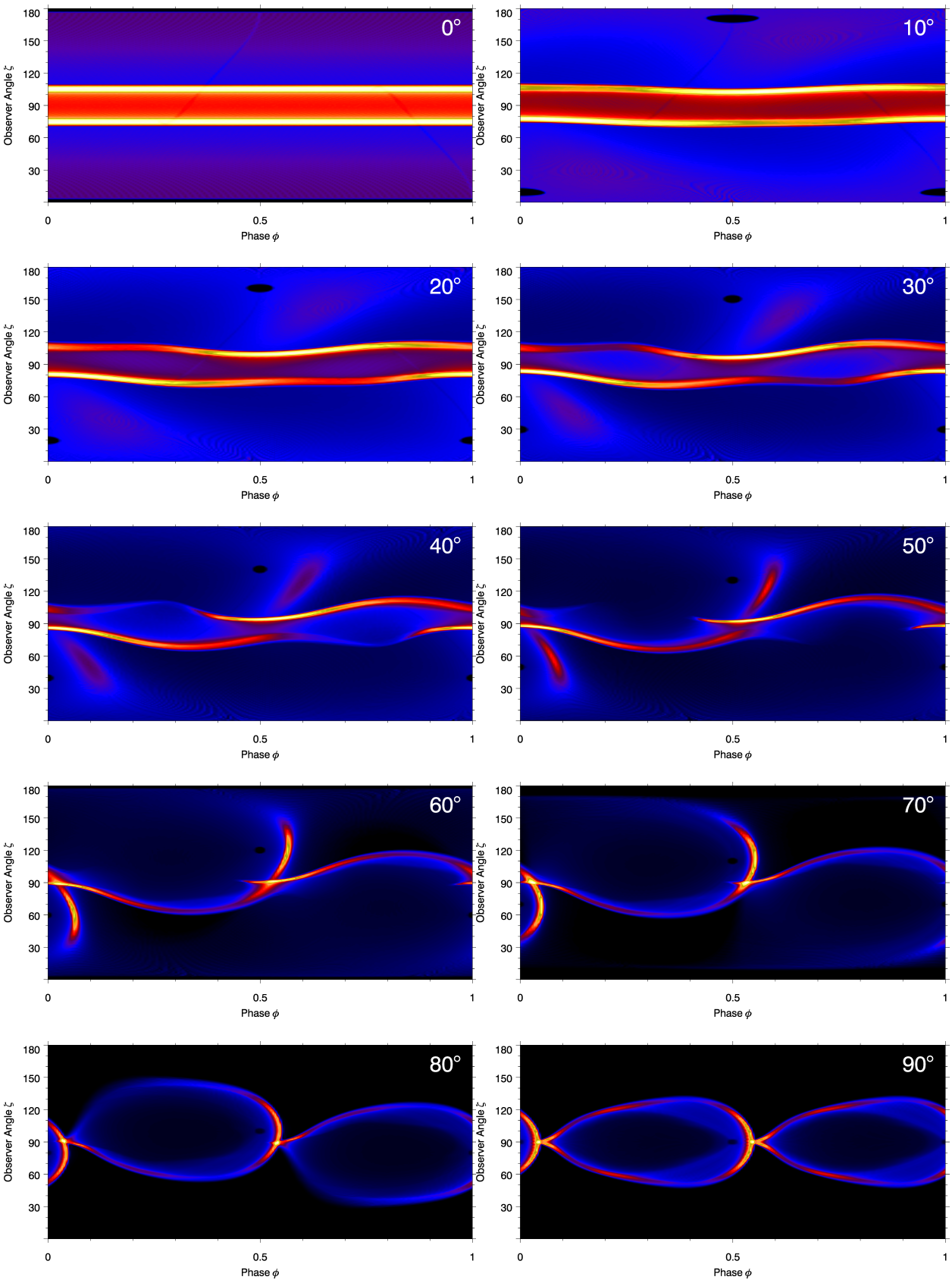


Figure 4.8: Phaseplots for α between 0° and 90°, stepping in increments of 10°, for the TPC case, assuming a static dipole magnetic field structure.

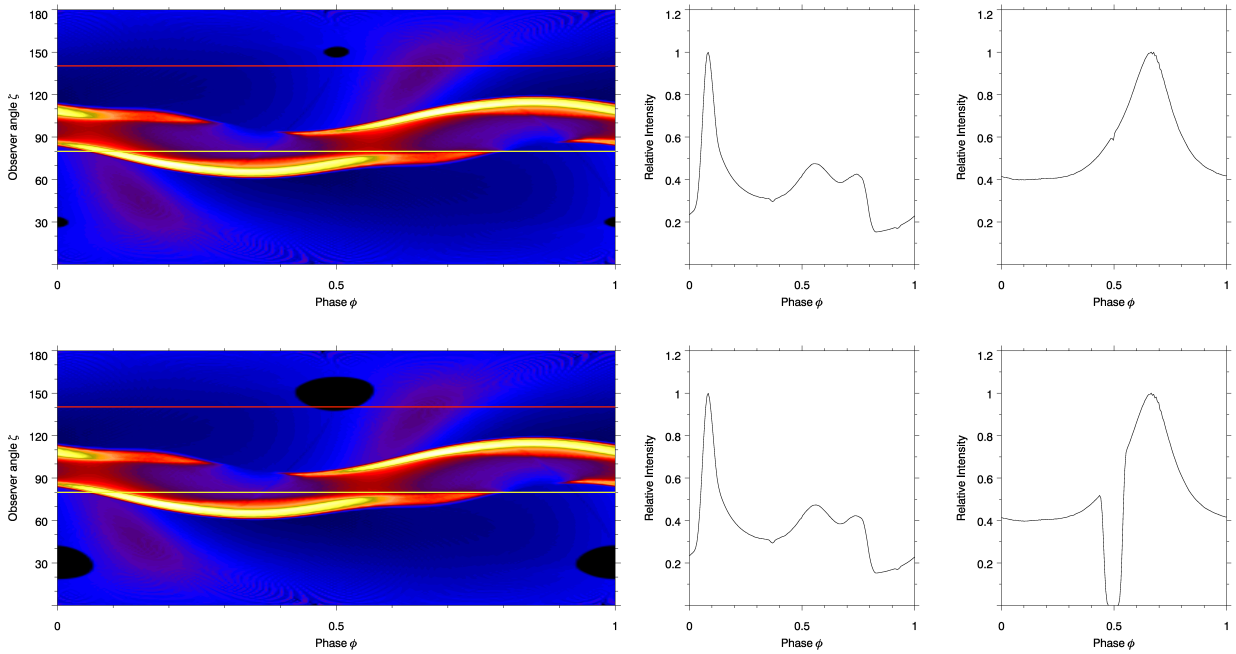


Figure 4.9: The effect of the pulsar period on the phaseplots for canonical (top, $P = 0.16\,\mathrm{s}$) and millisecond (bottom, $P = 0.016\,\mathrm{s}$) pulsars at low α ($= 30°$). In both cases the cuts are at $\zeta = 80°$ (left-most LC, yellow line) and $140°$ (right-most LC, red line). The dip in intensity on the LC at $\phi = 0.5$ is due to the PC being cut.

spot on the phaseplot) is larger for a shorter P. This means that the feature has an effect on a larger range of ζ around $\zeta = \alpha$ in this case. The magnitude of the effect in terms of its range in ϕ, namely a dip in intensity on the LCs at $\phi = 0$, is also increased as the period is decreased. The rest of the LC structure remains unchanged. This behaviour can be understood as being due to the fact that the magnetic field structure scales with R_{LC} (and thus P), while R_{NS} does not. This means that a shorter P causes R_{NS} to be a larger fraction of R_{LC}. Hence the gap does not extend to the same low fractional altitude seen in the longer P case, and thus the PC appears larger on the phaseplot.

In the OG case one can only see an effect due to P when the geometry is such that the last open field line's footpoint on the perimeter of the PC is above the null-charge surface for a portion

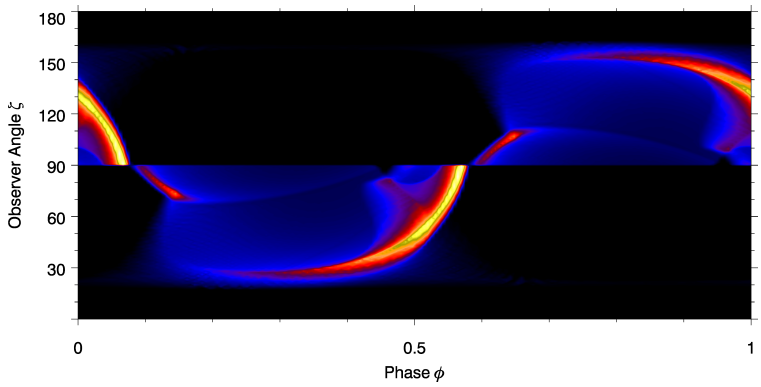


Figure 4.10: The effect of pulsar period on the predicted OG phaseplot. In this example a large value for α was chosen ($\alpha = 80°$) to illustrate under what kind of conditions the pulsar period would have an effect on the OG phaseplot for an MSP. This effect, which manifests itself in the form of an eroded semi-circle just interior to the caustic, can be appreciated by comparing this phaseplot to the one for $\alpha = 80°$ in Figure 4.3.

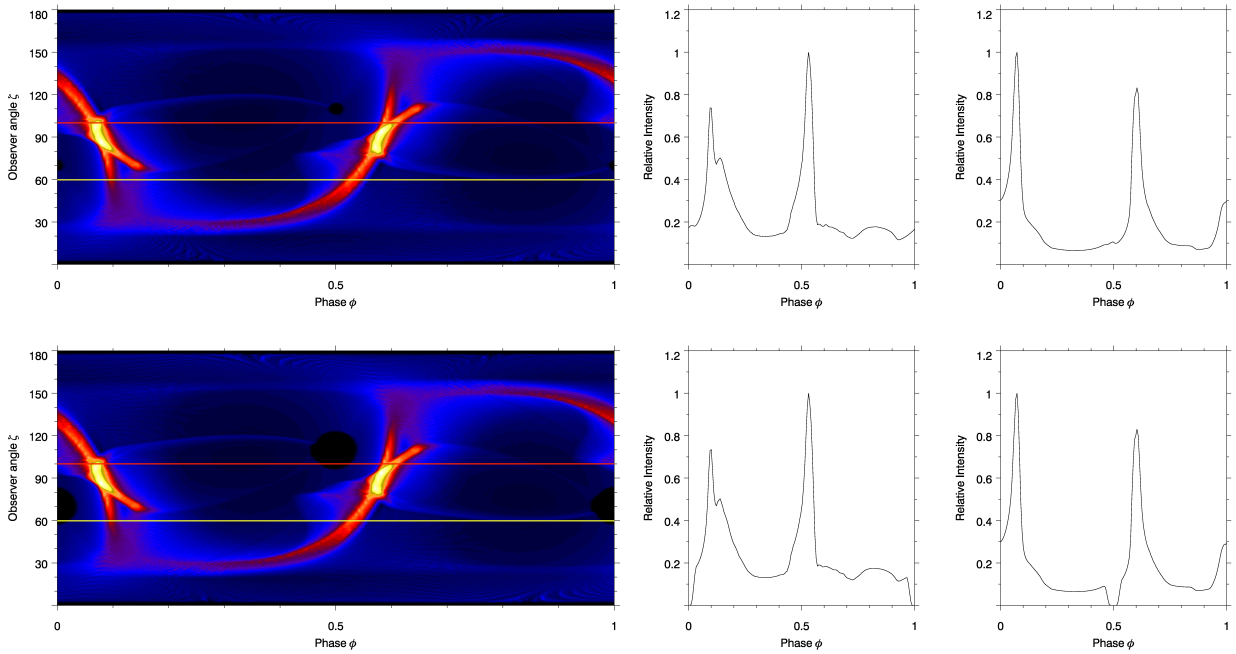


Figure 4.11: The effect of the pulsar period on the phaseplots for canonical (top, $P = 0.16\,\mathrm{s}$) and millisecond (bottom, $P = 0.016\,\mathrm{s}$) pulsars at high α ($= 70°$). In both cases the cuts are at $\zeta = 60°$ (left-most LC, yellow line) and 100° (right-most LC, red line). The dip in intensity on the LC at $\phi = 0.5$ is again due to the PC being cut.

of the PC. This can either happen at a large α, or at a very short period, or a combination of the two. The shorter the period, the larger the range of α around 90° over which the PC may have an effect on the OG phaseplots. Figure 4.10 illustrates one such case.

4.3.2 Maximum radial extension of the gap: R_{max}

Throughout this study it is assumed that emission originates in a thin gap along the last open field line, or just interior to it in the OG case, at radii starting at the stellar surface where $R_{\mathrm{min}} = R_{\mathrm{NS}}$ for the TPC case, at the null-charge surface $R_{\mathrm{min}} = R_{\mathrm{NCS}}$, in the OG case, and extending up to $R_{\mathrm{max}} = 1.2\ R_{\mathrm{LC}}$ (and a cylindrical radius $\rho_{cyl} < 0.95 R_{\mathrm{LC}}$). For completeness, the effect of a lower value of R_{max} is investigated in this section. Figure 4.12 shows phaseplots for the OG case with R_{max} ranging from $0.2\,R_{\mathrm{LC}}$ to $1.2\,R_{\mathrm{LC}}$ in steps of $0.2\,R_{\mathrm{LC}}$. As the value of R_{max} increases, the portion of the phaseplot over which emission is visible, increases. This doesn't occur to the same extent in every direction around the magnetic pole, which is located at [0,70°] in Figure 4.12, and this increase is biased toward earlier phases with respect to the pole's location. Furthermore, this direction-preferential increase becomes larger as radiation originating from progressively higher altitudes is included. This is due to the effects of aberration and time-of-flight (see Section 3.4) being more pronounced farther from the rotation axis of the pulsar, where the corotation velocities approach the speed of light, leading to bunching of emission on the trailing field lines and a spreading in ϕ on the leading field lines. From about $R_{\mathrm{max}} = 0.6 R_{\mathrm{LC}}$ onward the caustic's position in phase doesn't significantly change. This attribute of progressively higher altitude emission contributing to progressively larger portions of the phaseplot means that there exists a kind of "altitude to distance from the pole" mapping in the γ-ray model, and that very broad profiles correspond to emission geometries having comparatively large values for R_{max}.

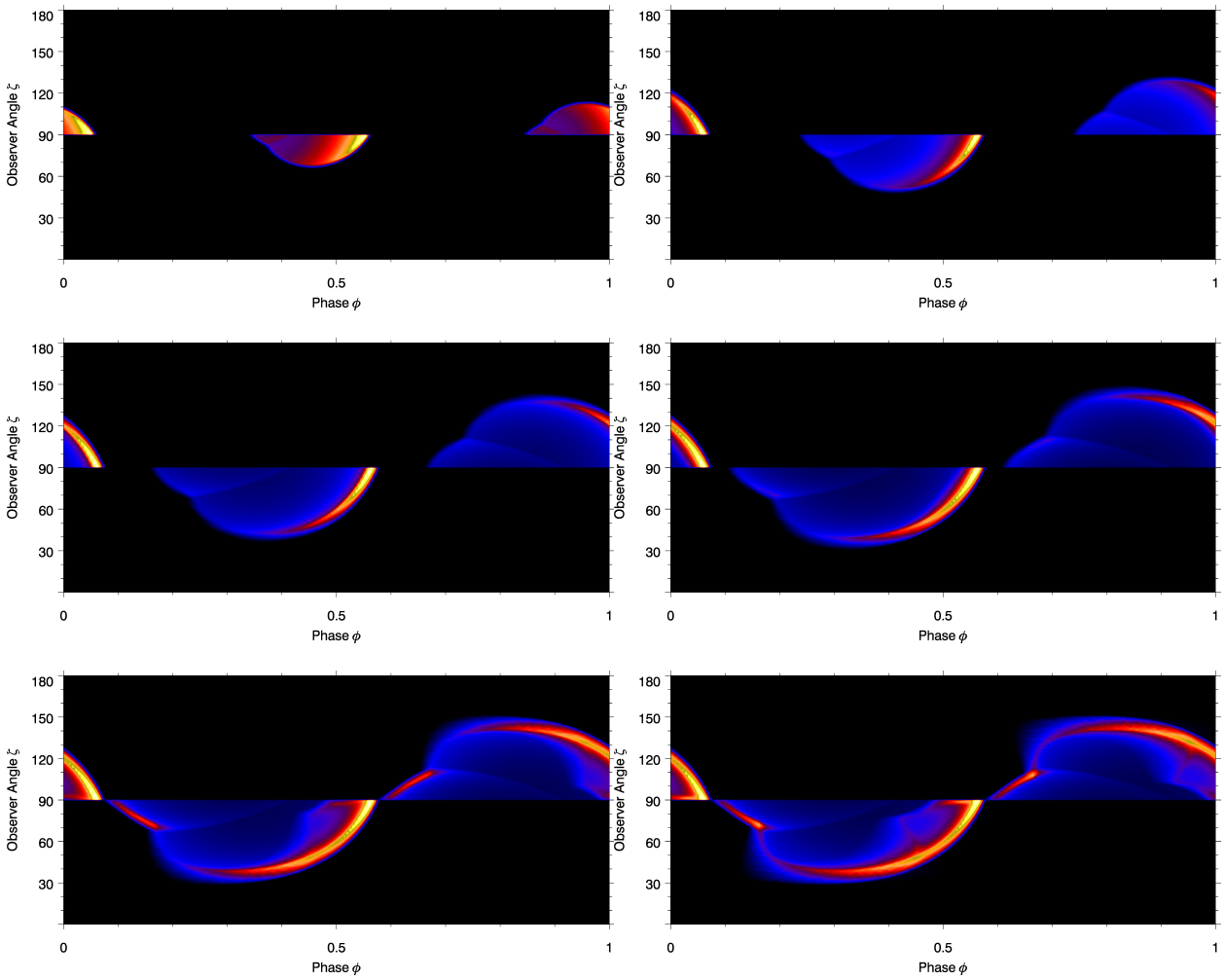


Figure 4.12: Phaseplots for the OG model with $R_{\rm max}$ increased in steps of $0.2R_{\rm LC}$ from $R_{\rm max} = 0.2R_{\rm LC}$ to $1.2R_{\rm LC}$.

Figure 4.13 shows phaseplots for the same set of $R_{\rm max}$ values for the TPC model. A striking feature of the TPC phaseplot when $R_{\rm max} = 1.2\,R_{\rm LC}$ is that almost the whole phaseplot is filled with emission. By comparing the last panels of Figure 4.13 and Figure 4.12, one can get an idea of which emission originates below the null-charge surface in the TPC case.

4.3.3 Gap width and position

Figure 4.14 shows TPC phaseplots, and accompanying LCs, corresponding to different gap widths ranging from 50% to 10% of the PC angle, generated by keeping the centre of the gap fixed at 75% of the PC angle, and varying the locations of the inner and outer edges of the gap. The most notable effect is that a larger gap corresponds to a broader caustic on the phaseplot. This means that sharper peaks are produced when thinner gaps are assumed.

Figure 4.15 illustrates what happens when the gap width is kept constant (10% of the PC angle in this case), but the gap position is changed. When moving closer to the magnetic axis, the first effect is the appearance of curved bands devoid of emission directly after the caustic in phase. The second effect is that peaks on the LCs shift later in phase as the gap is moved farther from the magnetic pole. This effect is most relevant when it is noted that the OG model assumes a gap

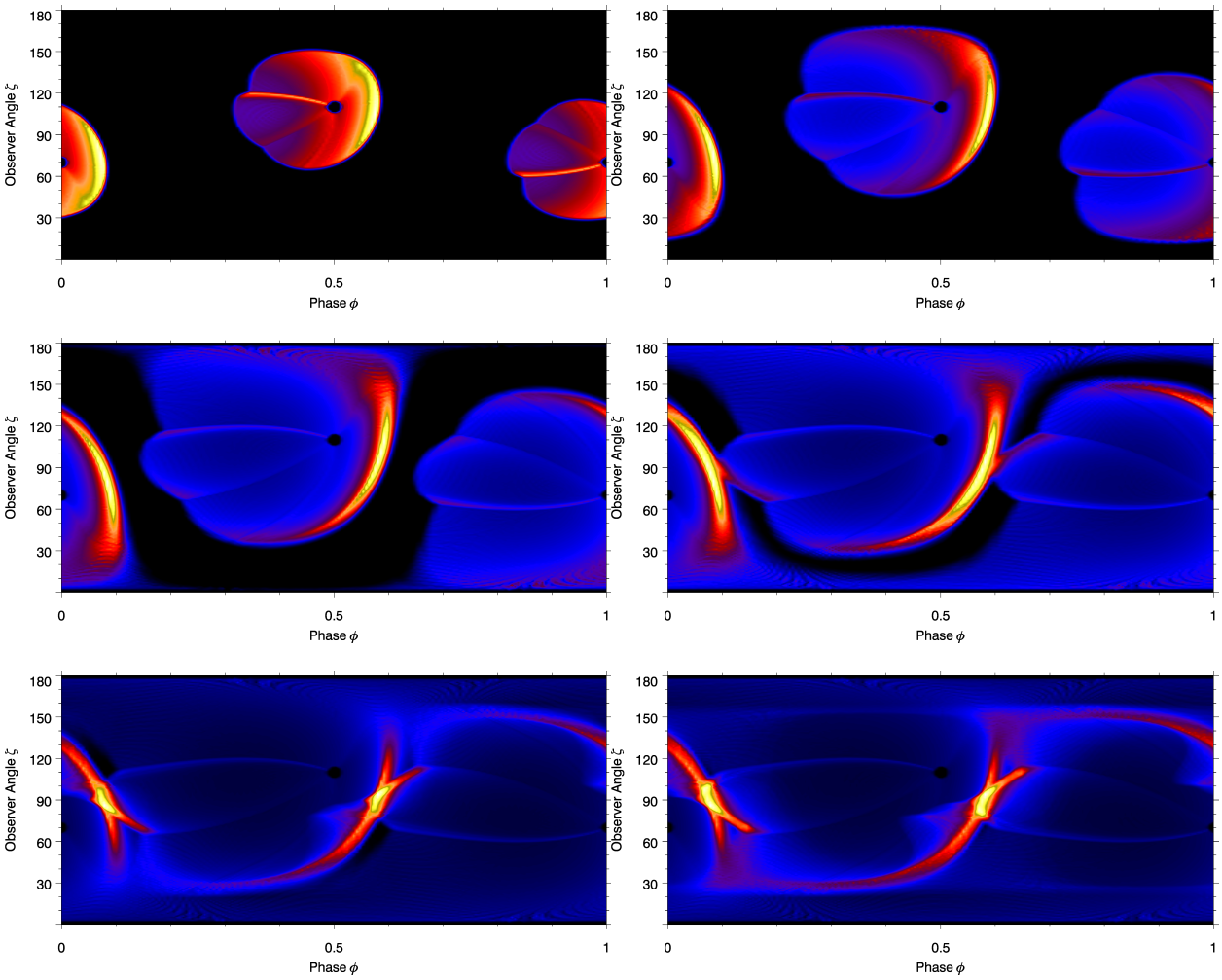


Figure 4.13: Phaseplots for the TPC model with $R_{\rm max}$ increased in steps of $0.2R_{\rm LC}$ from $R_{\rm max} = 0.2R_{\rm LC}$ to $1.2R_{\rm LC}$.

position which is closer to the magnetic pole than that assumed by the TPC model.

4.4 Radio parameters

The radio model used in this study is simple in comparison to the γ-ray models used. As discussed in Section 3.3, the radio emission originates from an annulus located at a fixed, parameter-dependent height given by Eq. (3.5). The predicted radio emission normally manifests itself in the form of a ring on the phaseplot. As this emission occurs at relatively low altitudes compared to $R_{\rm LC}$, the rotation of the pulsar doesn't have a very significant effect other than the distortion due to the notch in the PC boundary. The notch is clearly visible on the phaseplots, and is located on the earlier edge of the radio emission ring. Taking the frequency as fixed at 1.4 GHz, only the pulsar period and period derivative can affect how the phaseplots look in this model.

The effect the period has on the phaseplots is quite simple, with longer P corresponding to smaller rings on the phaseplots as shown in the left column of Figure 4.16. This is to be expected as the size of the light cylinder (and thus the size of the torus formed by the closed $\boldsymbol{B}$ region) increases more rapidly (which is proportional to P) than the value of $r_{\rm KG}$ does (which is proportional to $P^{0.3}$). This means that, in terms of $R_{\rm LC}$, the emission originates from relatively lower heights at

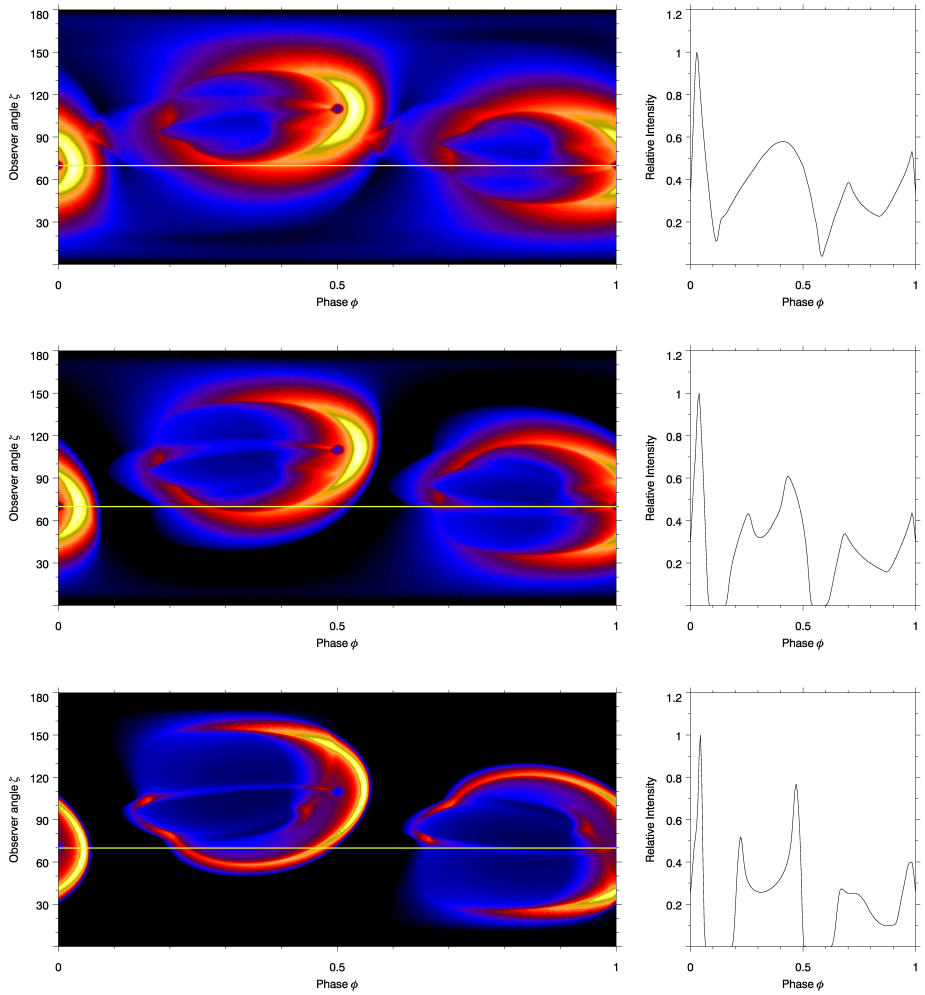


Figure 4.14: The effect of the TPC gap width on the produced phaseplots, with accompanying LCs. In all three sets $\alpha = 70°$, $\zeta = 70°$, and the centre of the gap is at 75% of the PC angle. In the *top* set the gap width is 50% of the PC angle, while in the *middle* and *bottom* sets it is 30% and 10% of the PC angle, respectively. There is a tendency for LC peaks to become sharper as the gap width is decreased. Furthermore, the caustic emission bunches along the original outer edge of the caustic structure as the gap width is decreased. This causes the original broad single peak to split into two peaks.

longer periods. The effect on the atlas is that the diagonal band along which radio emission is visible is wider at shorter periods, and vice versa.

The effect of the period derivative seems to be quite small when compared to that of the period. The values for $\dot{P}$ covered in the right column of Figure 4.16 span most of the range of values possible for canonical pulsars (see Figure 2.1) without significantly changing the size of the ring on the phaseplots, as compared to the period. Larger $\dot{P}$s correspond to larger rings.

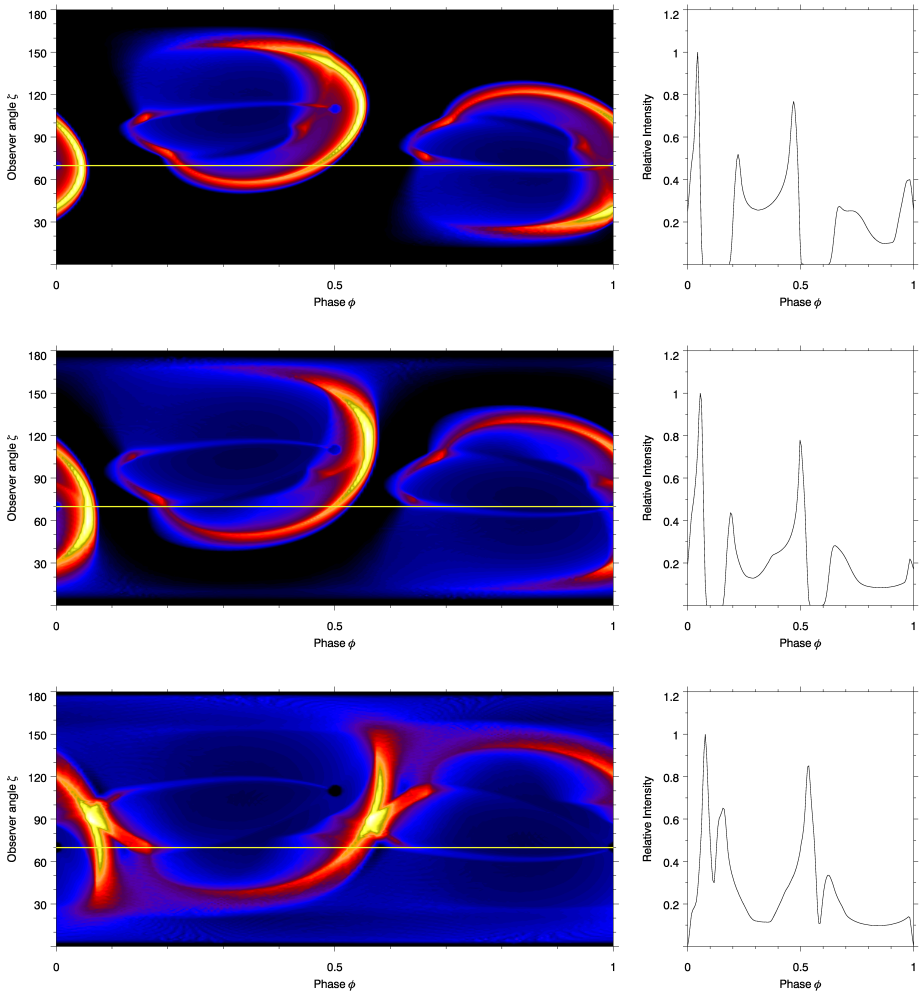
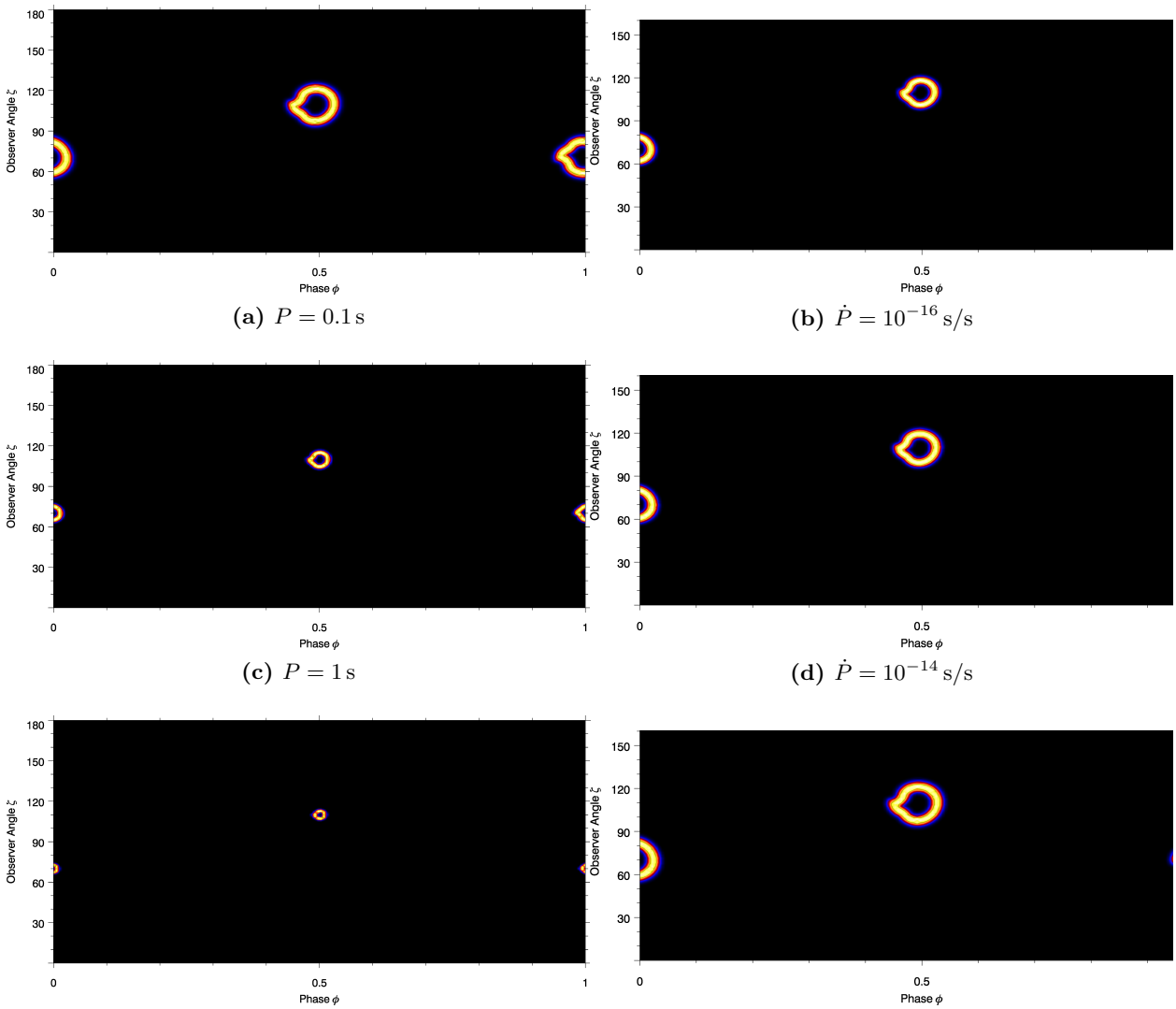


Figure 4.15: The effect of the TPC gap position on the produced phaseplots, with accompanying LCs. In all three sets $\alpha = 70°$, $\zeta = 70°$, and the gap width is 10% of the PC angle. In the *top* set the gap's inner boundary is located at 70% of the PC angle, while in the *middle* and *bottom* sets it is located at 80% and 90%, respectively. The peaks in the LCs move to earlier and later phases as the gap is moved closer to the last open field line. Furthermore, the closer the gap is located to the last open field line, the larger the portion of (α, ζ) space filled with emission, leading to more off-peak emission in the LCs.



(a) $P = 0.1\,\mathrm{s}$ **(b)** $\dot{P} = 10^{-16}\,\mathrm{s/s}$

(c) $P = 1\,\mathrm{s}$ **(d)** $\dot{P} = 10^{-14}\,\mathrm{s/s}$

(e) $P = 5\,\mathrm{s}$ **(f)** $\dot{P} = 10^{-12}\,\mathrm{s/s}$

Figure 4.16: The effects of P (left column) and $\dot{P}$ (right column) on the radio phaseplots. For all phaseplots $\alpha = 70°$. As P is increased (from top to bottom), the radius of the ring on the phaseplots decreases, which means that radio emission will be visible over a smaller range of ζ values. Increasing $\dot{P}$ has the opposite effect, but to a much lesser degree, resulting in larger ζ ranges over which radio emission is visible at higher $\dot{P}$.